

**OPEN ACCESS**

## Structural Influence of the Anode Materials towards Efficient Zn Deposition/Dissolution in Aqueous Zn-Iodide Flow Batteries

To cite this article: Monalisa Chakraborty *et al* 2021 *J. Electrochem. Soc.* **168** 040532

View the [article online](#) for updates and enhancements.



### 240th ECS Meeting

Oct 10-14, 2021, Orlando, Florida

**Register early and save  
up to 20% on registration costs**

Early registration deadline Sep 13

**REGISTER NOW**





# Structural Influence of the Anode Materials towards Efficient Zn Deposition/Dissolution in Aqueous Zn-Iodide Flow Batteries

Monalisa Chakraborty,<sup>1,2</sup> Sebastián Murcia-López,<sup>1,z</sup>  Joan Ramón Morante,<sup>1,3</sup> and Teresa Andreu<sup>1,3,z</sup>

<sup>1</sup>Catalonia Institute for Energy Research (IREC), Sant Adrià de Besòs, 08930, Spain

<sup>2</sup>Universitat Autònoma de Barcelona (UAB), Plaça Cívica, Bellaterra 08193, Spain

<sup>3</sup>University of Barcelona (UB), Barcelona 08028, Spain

Zinc-iodide flow battery (ZIFB) is one of the best potential candidates for future grid-scale energy storage, due to its eye-catching features of benign, high energy density and non-corrosive nature. However major investigations have not done yet on the negative electrode of this battery where the Zn deposition/dissolution mechanism takes place, which may have an impact on the battery performance. Herein, we have reported a comparative study of different carbon-based anodes which are conventional graphite felt, carbon paper and graphite foil. Single-cell charge/discharge performances among these three different anodes depicts that the cell with planar, hydrophilic graphite foil anode is showing the best energy efficiency and the lowest cell resistance among the carbonaceous electrodes. Zinc dissolution process during discharge process seems to be the bottleneck for having a stable cell, which was corroborated by the use of a Zn foil anode that shows excellent efficiencies along the successive cycles.

© 2021 The Author(s). Published on behalf of The Electrochemical Society by IOP Publishing Limited. This is an open access article distributed under the terms of the Creative Commons Attribution 4.0 License (CC BY, <http://creativecommons.org/licenses/by/4.0/>), which permits unrestricted reuse of the work in any medium, provided the original work is properly cited. [DOI: 10.1149/1945-7111/abf4ee]

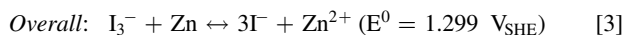
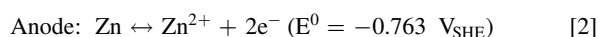
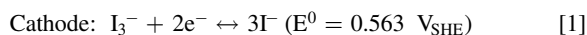


Manuscript submitted January 22, 2021; revised manuscript received March 18, 2021. Published April 27, 2021.

Among various electrochemical energy storage technologies, redox flow batteries (RFBs) are considered as one of the promising candidates for large-scale stationary storage of energy generating from renewable, clean power sources such as solar and wind.<sup>1-4</sup> Unlike conventional batteries, flow batteries have a unique architecture of upscaling energy and power separately by storing redox-active species in external reservoirs.<sup>5</sup> The most researched all-vanadium redox flow battery has found a commercial deployment featuring qualities like long life span, good electrochemical reversibility,<sup>6-8</sup> but are limited by the low energy density (<25 Wh·L<sup>-1</sup>) and low concentration of vanadium ions (2.0 M in the electrolytes to avoid precipitations).

With the prospect of having high energy density and cost-effectiveness, alternative flow batteries like zinc-based aqueous RFBs are quite appealing because of earth-abundant, benign Zn is used as redox-active material as well as the two-electron transfer is possible in the half-cell reactions. Compared to the popular redox couple of Zn-based RFBs, Br<sup>-</sup>/Br<sub>2</sub>, I<sup>-</sup>/I<sub>3</sub><sup>-</sup> redox couple is most promising since I<sub>2</sub> is non-toxic and less corrosive than Br<sub>2</sub>.<sup>9</sup>

B. Li et al. firstly reported a zinc-iodine flow battery (ZIFB) with a high discharge energy density of 167 W·h·L<sup>-1</sup> catholyte based on ZnI<sub>2</sub> aqueous electrolyte and pristine graphite felts electrodes.<sup>10</sup> The battery is based on the following redox reactions:



It is worth noting that the relatively low thermodynamic potential of this system compared to the actual values required in water electrolyzers, makes ZIFB a promising candidate for alternative devices integrating photoelectrodes.

The general schematic of ZIFB is shown in Fig. 1. The two active redox couples, Zn<sup>2+</sup>/Zn (s) from the negative side and I<sup>-</sup>/I<sub>3</sub><sup>-</sup> from the positive side respectively, are taking part in the redox reactions described in Eqs. 1–2, where Eq. 1 follows a two-step process of redox reaction (Eq. 4) and complexation (Eq. 5).<sup>11-13</sup>



During charging, metallic Zn is reductively electrodeposited on the anode surface while triiodide ions are formed by oxidation of iodide in the positive half-cell. The reverse process occurs upon discharge.

Li and Liu et al. introduced a metal-organic framework (MOF) into the graphite felt (GF) surface as a highly active electrocatalyst, served as the positive electrode. This MOF-GF electrode shows higher energy efficiency compared to the pristine GF.<sup>14</sup> Higher energy density of 202 W·h·L<sup>-1</sup> catholyte has been achieved by Weng et al. by introducing bromide ion (Br<sup>-</sup>) as a complexing agent to stabilize iodine molecules and free up the iodide ions which leads to increase capacity.<sup>13</sup> Other authors have developed aqueous Zn-I<sub>2</sub> batteries by using encapsulated iodine molecules in micro-porous carbon as positive electrode.<sup>15-17</sup> This approach aims to avoid I<sub>3</sub><sup>-</sup> formation and work with I<sub>2</sub> as active species.

Other few studies have been done so far on aqueous Zn-I<sub>2</sub> static/flow batteries. For example, Xie et al. described a high power density single-flow ZIFB by replacing the ZnI<sub>2</sub> electrolyte by KI and ZnBr<sub>2</sub> along with sealing the positive compartment and introducing low-cost porous polyolefin membrane.<sup>18,19</sup> Zhang et al. designed a high potential Zn-I<sub>2</sub> alkaline FB by tuning pH of the anolyte from acid to basic,<sup>20</sup> whereas Ito et al. achieved over 90% coulombic efficiency after addition of propylene carbonate in the electrolyte which forms hydrophobic polyiodide complex during cathodic oxidation in a Zn-I<sub>2</sub> single FB without cation exchange membrane.<sup>21</sup> Lu et al. worked on nitrogen and sulfur-doped 3D porous graphene foams as both cathode and anode which enable rapid ion transport as well as reversible Zn plating/stripping process in anode.<sup>22</sup>

Overall, so far studies on aqueous Zn-I<sub>2</sub> batteries have been mainly focused on improving cathode materials, I<sup>-</sup>/I<sub>3</sub><sup>-</sup> redox chemistry, design of single flow battery without the use of cation exchange membrane.<sup>13-21</sup> Few investigations have done so far on the impact of Zn plating/stripping on the cell electrochemical performance. Chamoun et al. demonstrated that electrochemically synthesized hyper-dendritic nanoporous Zn foam anode exhibits excellent capacity retention over 100 cycles which could be helpful for Zn-based rechargeable batteries.<sup>23</sup> Jiang et al. reported first-principle calculations of Zn adsorption mechanism on carbon surfaces and found that by modifying the carbon surface by creating single

<sup>z</sup>E-mail: smurcia@irec.cat; tandreu@ub.edu

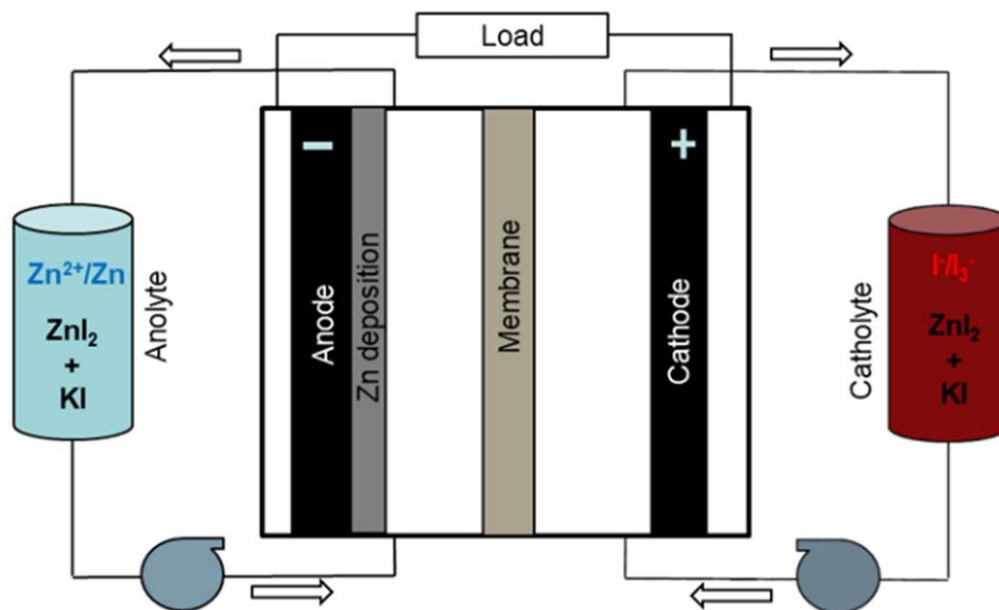


**Figure 1.** Schematic diagram of Zn-iodide flow battery (ZIFB).

vacancies it is possible to achieve uniform Zn deposition on GF electrode.<sup>24</sup> Hosseini et al. recently reported that the addition of dimethyl sulfoxide (DMSO) as a potential additive in the anolyte of alkaline Zn-air FB, enhances Zn dissolution from the surface of the anode, which improves discharge capacity and cyclability.<sup>25</sup> However, so far from most of the published literature, it is clear that the negative side of the aqueous Zn-based flow batteries is an aspect that has been often overlooked. Whereas negative electrode plays a significant role in the cell cycling performance as Zn plating/stripping takes place during charge/discharge cycling.

Based on the points of the effective Zn deposition/dissolution to the anode surface, herein, we have carried out comparative studies of different carbon-based anodes such as conventional porous graphite felt (G-felt), carbon paper (C-paper) and planar graphite foil (G-foil) to understand the influence of the anode materials in the ZIFB full-cell cycling performance. We have carried out half-cell electrodeposition tests following SEM characterization to gather ideas about the change of Zn plating microstructure and morphologies based on the physical properties of the anode; contact angle test to verify the electrolyte wettability on anodes that helped to understand the full-cell cycling of the anodes. This approach might give a better understanding of choosing suitable anode in future research on Zn-I<sub>2</sub> flow batteries.

### Experimental

**Lab-scale ZIFB single-cell preparation.**—The ZIFB single cell was assembled by using an in-house designed flow cell setup (Fig. 2). Electrodes of 10 cm<sup>2</sup> geometric area were assembled by sandwiching commercially available Nafion® 117 membrane in between two half-cell compartments. In anode compartment, graphite felt (Sigracell® GFA 1.5 EA, 1.5 mm thick), carbon paper (Toray® TGP-H-60, 0.18 mm thick), graphite foil (Alfa Aesar®, 0.5 mm thick) or Zn metal foil (Goodfellow®, 0.5 mm thick) were used as anodes. Titanium metal plate was used as a negative current collector. Around 4 mm space was kept between the anode surface and membrane for the metallic Zn deposition. In the cathode compartment, two stacked graphite felts were used as the cathode in contact with a graphite plate as positive current collector. All graphite felts were thermally pre-treated at 420 °C for 10 h using a ramp rate of 5 °C min<sup>-1</sup> in air. Carbon paper and graphite foil were used as received, without pre-treatment. Viton® gaskets were used in

between each component to avoid the electrolyte leakage. Electrolyte was prepared at room temperature by mixing 1.5 M ZnI<sub>2</sub> (98.0%, Aldrich) and KI (99.5%, Sigma Aldrich) (1:1) in aqueous solution (milli-Q ultrapure water). The cell was connected to 10 mL of electrolyte reservoirs on each side. Electrolyte was circulated to the cell by a peristaltic pump (Masterflex L/S series) through Tygon® tubing at a fixed flow rate of 13 mL·min<sup>-1</sup> (Fig. S1 (available online at [stacks.iop.org/JES/168/040532/mmedia](https://stacks.iop.org/JES/168/040532/mmedia))).

The mixing of potassium iodide (KI) along with ZnI<sub>2</sub> (1:1) as the electrolyte provides enough free I<sup>-</sup> ions in the solution to equilibrate both compartments (Eq. 3 and supporting information-theoretical capacity calculation). However, according to Eq. 4, just 2/3 of I<sup>-</sup> ions are taking part in the charging process which corresponds to ~67% state of charge (SOC), while the remaining I<sup>-</sup> forms highly soluble polyiodide, I<sub>3</sub><sup>-</sup> (Eq. 5). Thus, if the charging continues to higher SOC, there will be the formation of insoluble solid I<sub>2</sub> which can further lead to interrupt the electrolyte flow by blocking the tubing side following capacity loss.<sup>19</sup>

**ZIFB single cell test.**—The electrochemical performance of ZIFB single cell was carried out by traditional charge/discharge tests under galvanostatic conditions operating at 10 and 20 mA·cm<sup>-2</sup> using a Biologic® VMP3 potentiostat. The charge was controlled by both upper cut-off voltage (1.6 V) and 67% of theoretical capacity. Coulombic (CE), voltage (VE) and energy (EE) efficiencies were calculated by Eqs. 6–8, where  $Q$  is the battery capacity and  $V$  is the average cell potential during the charge/discharge.

$$CE = Q_{\text{discharge}}/Q_{\text{charge}} \quad [6]$$

$$VE = V_{\text{discharge}}/V_{\text{charge}} \quad [7]$$

$$EE = CE \cdot VE \quad [8]$$

Electrochemical Impedance Spectroscopy (EIS) measurements were conducted at open-circuit conditions within a frequency range of 200 kHz to 100 mHz and AC perturbation of 10 mV of amplitude, to investigate the series resistance ( $R_s$ ) of the cell assembled with all the three anodes.

Current-interrupt method was used to estimate the ohmic resistance ( $R_{\text{ohm}}$ ) with the three electrodes after polarization. This technique, commonly applied in fuel cells, is based on the transient

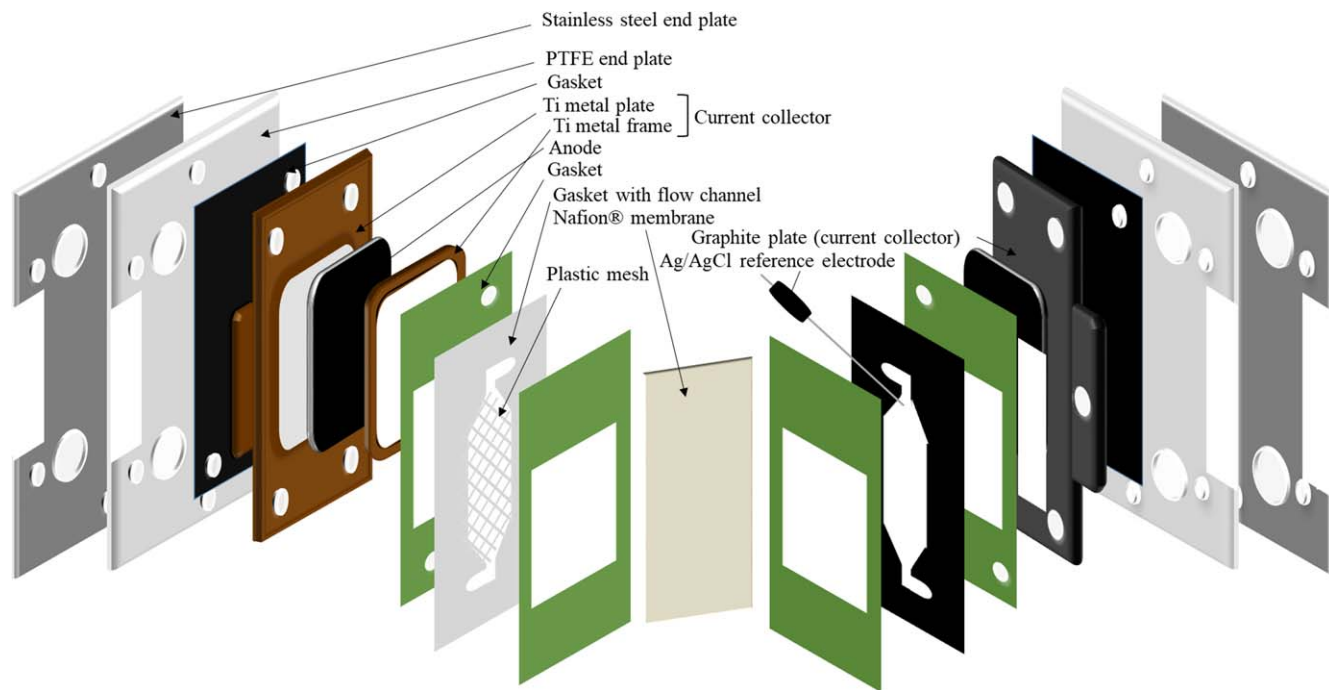


**Figure 2.** Lab-scale assembling of single-cell ZIFB.

voltage response after current interruption (i.e., changing from polarization conditions to relaxation mode in a short time period).<sup>26</sup> More details are provided in the Supporting Information (Fig. S2).

**Characterization.**—The zinc electrodeposition tests were done in a three-electrode cell. G-felt, C-paper, or G-foil anodes of 1 cm<sup>2</sup> area were used as working electrodes, platinum mesh as counter electrode and Hg/Hg<sub>2</sub>SO<sub>4</sub> as the reference electrode. Total charge was applied of about 193 C·cm<sup>-2</sup> under current densities 10 and 20 mA·cm<sup>-2</sup>.

Structural analysis with X-ray diffraction (XRD) was performed by using a Bruker D8 Advance diffractometer equipped with a Cu K $\alpha$  radiation (0.15417 nm) source, a LYNXEYE super speed detector and a Ni filter.

The morphology and nanostructure of anodes were characterized by Zeiss Auriga 60 field emission scanning electron microscope (FE-SEM) with an acceleration voltage of 5 kV.

Sessile drop technique (dataphysics instruments, model no. TBU90E) was performed to understand the wetting behavior of the electrolyte on the anode surface. 10  $\mu$ L of droplet was applied on the sample's surface.

To identify the graphitic structural properties of different anodes, Raman spectroscopy measurements were carried out by using Horiba Scientific Superhead iHR320 spectrometer equipped with a 532 nm excitation laser source.

## Results and Discussion

### Electrochemical performance of ZIFB with different anodes.—

Figure 3a represents charge-discharge voltage curves of full-cell assembled with graphite felt as the cathode and different anodes. Cycling was done with 1.5 M ZnI<sub>2</sub>: KI (1:1) electrolyte at the current density of 10 mA·cm<sup>-2</sup>. It can be seen that the cell assembled with G-felt anode is showing the lowest discharge capacity compared to the cells assembled with C-paper and G-foil anodes. Besides, cells with G-felt and C-paper show higher internal resistances compared to the cell with G-foil. Cycling efficiencies are shown in Fig. 3b. As it can be seen, CE of the cell with G-felt anode decreases gradually upon cycling which leads to EE decay, although VE does not show any significant decay. The cell using C-paper anode maintains stable

performance without a steep drop in any of the efficiencies. Finally, the cell with G-foil anode exhibits excellent VE among all the three anodes. Additionally, along with approximately consistent CE values throughout the cycling period, this cell is showing the best EE compared to the other two cells in overall.

In Table I the values of  $R_{ohm}$  estimated from the current-interrupt method at two current densities (10 and 20 mA·cm<sup>-2</sup>) are summarized. These values are calculated based on the average voltage drops at the end of the charge during all the cycles, and are associated to the ohmic drop after relaxation when changing from polarization to open-circuit conditions. Similar  $R_{ohm}$  values are obtained with independence on the applied current density. In general, the G-foil exhibits the lowest ohmic resistance, associated to a lowest voltage drop after relaxation, while both G-felt and C-paper present higher values. In particular, the C-paper has the highest resistance despite its intrinsic good electrical conductivity (<0.08  $\Omega$ ·cm), which can be explained by its poor wettability, as indicated later. These results agree with the obtained voltage efficiencies, which were lower and similar with the two porous electrodes along all the cycles.

EIS tests at OCV were carried out to investigate the series resistance ( $R_s$ ) of the cell assembled with all the three anodes. Figure S3 depicts the Nyquist impedance plots of the ZIFB single-cell with anodes; G-felt, C-paper and G-foil respectively in 1.5 M ZnI<sub>2</sub>: KI (1:1) electrolyte. Here,  $R_s$  is the combination of electrolyte resistance, electrode resistance and interface resistance. The  $R_s$  values of these anodes could be seen clearly in the enlarged plot (Fig. S3b).  $R_s$  is lowest in G-foil by taking into account a slight difference with C-paper, and highest in G-felt. Therefore, this  $R_s$  value could provide a preliminary statement about the electrical conductivities of these three anode materials where G-foil is showing the highest electrical conductivity.

Additionally, the XRD measurement of the cycled G-foil (Fig. S7) clearly shows only metallic Zn (JCPDS 041-1487) along with two peaks of weak intensities which belong to graphite (JCPDS 004-0831). Both structures belong to the hexagonal crystalline group and exhibit certain orientation towards the [002] direction. This pattern proves that solid Zn is the only dominant product which is reversibly deposited on the G-foil anode.

For further comparing the graphitic structures and crystalline properties of these anode materials, we performed Raman spectroscopy

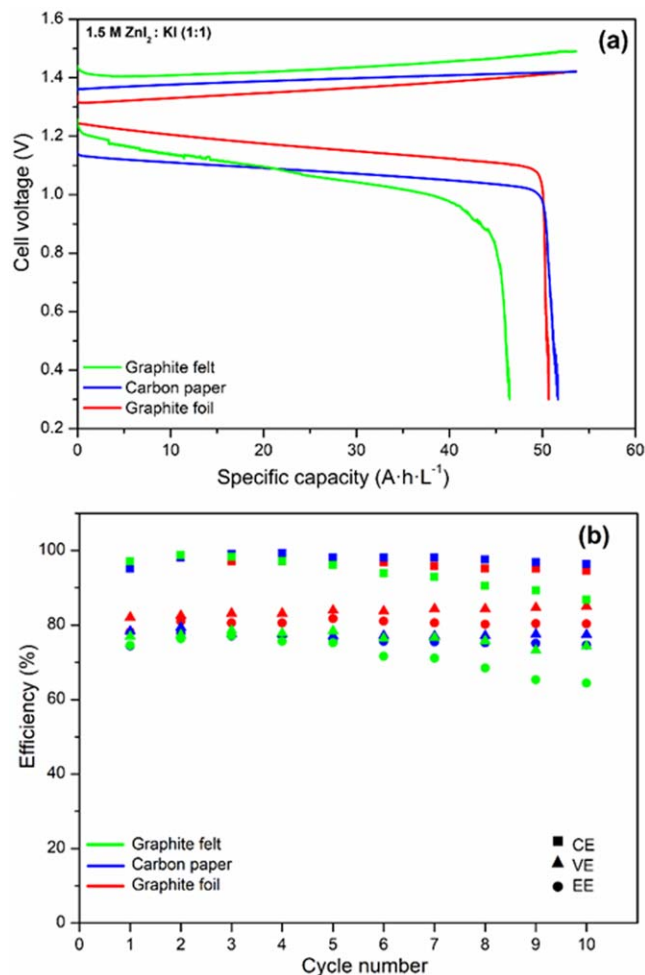


**Figure 3.** Comparison of (a) charge-discharge voltage curves of 10th cycle and (b) cycling performances for efficiencies of the full-cell of graphite felt, carbon paper and graphite foil as anode and graphite felt as cathode at 1.5 M  $\text{ZnI}_2$ : KI (1:1) at a current density of  $10 \text{ mA}\cdot\text{cm}^{-2}$ .

measurements. Figure S4 illustrates the Raman spectra of G-felt (thermally-treated), C-paper and G-foil. The first-order Raman spectrum exhibit defect/disordered (D), graphitic (G) and overtone (2D) bands at around  $1340$ ,  $1575$  and  $2700 \text{ cm}^{-1}$  (these bands are slightly shifted in each material), respectively. It can be clearly seen that the intensity of the D band is higher than the G band in G-felt. This proves the presence of defects associated to  $\text{sp}^3$  hybridization by breaking crystal symmetry (C–C stretching bond), and amorphous structure. On the other side, the C-paper spectrum exhibits G band of intensity higher than D band, which proves the tendency towards the oriented, graphitized structure. Finally, G-foil is showing a very sharp peak (G), about 4 times higher intensity than D, proving a highly graphitic structure. The graphitic peak to peak intensity ratios ( $I_D/I_G$ ) are calculated to be 1.28, 0.28 and 0.24 for G-felt, C-paper and G-foil,

respectively. Based on these ratios, it is possible to state the degree of crystallinity. As the intensities of D to G bands are inversely proportional to the crystallinity,<sup>27,28</sup> hence, the graphite foil is showing the highest degree of crystallinity while G-felt exhibits a more defective structure.

Therefore, in agreement with the values presented in Table I, G-foil exhibits a higher extension of the  $\text{sp}^2$  hybridization, which in turn might be associated to higher intrinsic electrical conductivity. Consequently, this crystalline, highly conductive nature of G-foil allows it to retain a stable CE throughout the full-cell cycling period (Fig. 3b). However, does not explain the difference of this anode with the C-paper.

**Zinc plating-stripping process with different anodes.**—To investigate the morphology and microstructure of Zn deposition on the anode surface, we carried out the electrodeposition on three different anodes with varied physical structure: G-felt (thermally-treated), C-paper and G-foil. An aqueous solution of 1.5 M  $\text{ZnI}_2$ : KI was used as the electrolyte. These chronopotentiometry measurements were performed up to 67% SOC which corresponds to surface charge density of  $193 \text{ C}\cdot\text{cm}^{-2}$  at two current densities, 10 and  $20 \text{ mA}\cdot\text{cm}^{-2}$ . In G-felt (Fig. 4a), all the fibers including those in the inner part of the electrode are covered with deposited Zn, as its highly porous nature allows the electrolyte to penetrate from the surface to the inner part of the substrate, leading to conformal deposition at  $20 \text{ mA}\cdot\text{cm}^{-2}$  (Fig. 4d). The highly hydrophilic nature of G-felt is shown in Fig. S3a, where after electrolyte drop deposition the materials became immediately wet and no contact angle was formed on the surface. In the case of C-paper, the fibers seem partially covered by non-uniform and discrete deposition at  $10 \text{ mA}\cdot\text{cm}^{-2}$  (Fig. 4b), and an accumulation of the Zn deposit present mostly on the surface at higher current density (Fig. 4e).

The difference in the deposition behavior between the three electrodes and in particular between the two porous substrates, G-felt and C-paper, can be ascribed to many factors. Albeit both materials consist on graphitized carbon (with differences in the graphitization degree), some differences on the functionalization of the surface can be expected to have influence on the electrochemical behavior. Additionally, obvious distinction in the microstructure also imply that both materials possess different electrochemical surface areas. In this sense, the thicker G-felt also exhibits higher porosity (close to 90% vs 78% for the C-paper) and lower density than the C-paper ( $< 0.1 \text{ g}\cdot\text{cm}^{-3}$  for G-felt and  $0.44 \text{ g}\cdot\text{cm}^{-3}$  for C-paper). These facts imply that the three substrates have potentially different areal capacities in the order of G-felt > C-Toray > G-foil, although in the present study only the geometrical area has been considered. Moreover, the partial PTFE coating of the C-paper, confers certain hydrophobic properties to this electrode with a contact angle of  $137^\circ$  (Fig. S5b), which does not allow the electrolyte to go into the bulk, and probably leads to the highest charge transfer resistance as seen in the Nyquist plot (Fig. S3a). The fact that C-paper has a limited wettability, introduces an additional overpotential which may explain the differences in the polarization resistance observed in the previous section, despite its high electrical conductivity. On the other side, SEM image of charged G-foil anode at  $10 \text{ mA}\cdot\text{cm}^{-2}$  (Fig. 3c) depicts identical particle-like deposition only on the surface as its planar structure does not allow electrolyte access to the bulk.

**Table I.** Comparison of  $R_{\text{ohm}}$  from current-interrupt method during charge process at two current densities of 10 and  $20 \text{ mA}\cdot\text{cm}^{-2}$ .

	Current density ( $\text{mA}\cdot\text{cm}^{-2}$ )	V1 (V)	V2 (V)	$\Delta V_{\text{ohmic}}$ (V)	Ohmic resistance ( $\Omega\cdot\text{cm}^2$ )
G-felt	10	$1.45 \pm 0.01$	$1.33 \pm 0.01$	$1.186 \pm 0.021$	$11.6 \pm 0.4$
	20	$1.56 \pm 0.04$	$1.34 \pm 0.01$	$1.069 \pm 0.012$	$11.2 \pm 0.3$
C-paper	10	$1.42 \pm 0.01$	$1.28 \pm 0.01$	$1.152 \pm 0.016$	$13.6 \pm 0.4$
	20	$1.54 \pm 0.005$	$1.30 \pm 0.003$	$1.030 \pm 0.002$	$12.2 \pm 0.4$
G-foil	10	$1.41 \pm 0.002$	$1.32 \pm 0.003$	$1.226 \pm 0.005$	$9.4 \pm 0.3$
	20	$1.47 \pm 0.003$	$1.30 \pm 0.003$	$1.163 \pm 0.056$	$8.4 \pm 0.3$

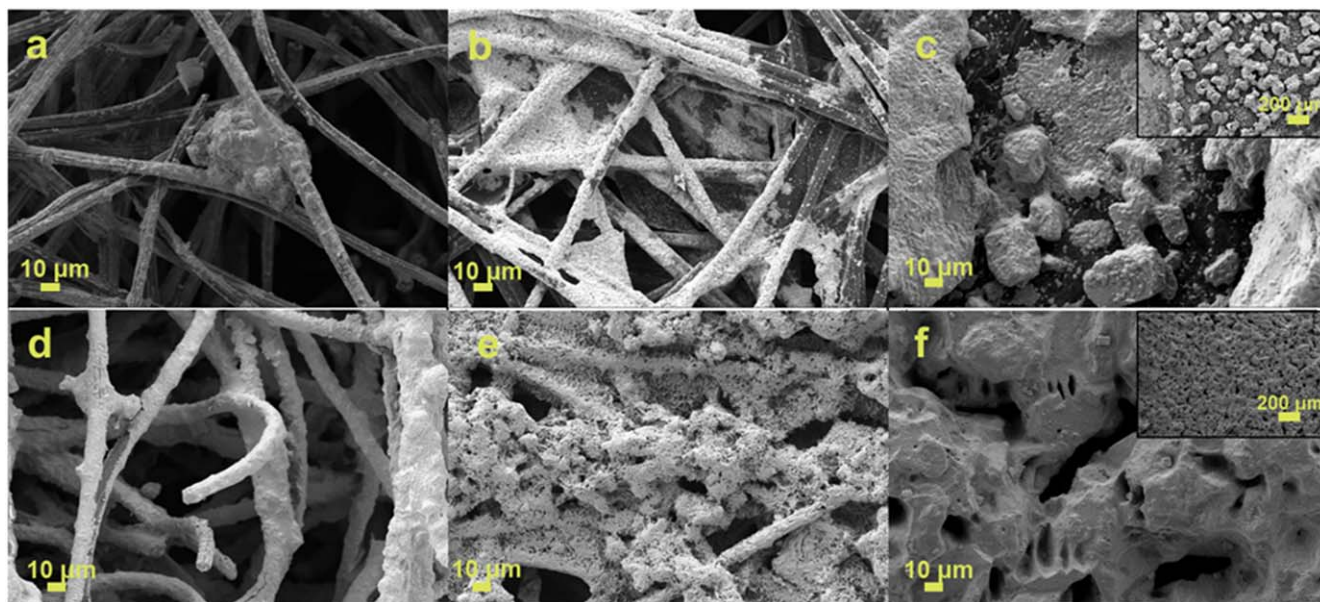


**Figure 4.** SEM images of (a)–(d) thermally-treated graphite felt, (b)–(e) pristine carbon paper and (c)–(f) pristine graphite foil; electrodeposited at  $193\text{ C}\cdot\text{cm}^{-2}$  at current density of  $10\text{ mA}\cdot\text{cm}^{-2}$  (a)–(c) and  $20\text{ mA}\cdot\text{cm}^{-2}$  (d)–(f) respectively.

G-foil is slightly hydrophilic, with a contact angle of  $77^\circ$ , and at  $20\text{ mA}\cdot\text{cm}^{-2}$  a much uniform and compact deposition than for C-paper, as seen in Fig. 4f (including inset picture at higher magnification). Overall, by comparing these three anodes it is obvious that morphology and pattern of Zn deposition vary according to the changes in the electrode microstructure.

Concerning the discharge, the pictures of these cycled anodes (Fig. S6) enlighten the reason for the difference between these cells cycling performance. A high amount of remaining Zn metal deposition can be seen on the G-foil (Fig. S6a) which means that the dissolution of the deposited products did not happen properly. After discharge, some remaining zinc is still deposited on the current collector side as well due to the porous nature of felt. This result of the improper dissolution of Zn could be correlated to the rapid capacity fading with cycling (Fig. 3b) due to the loss of  $\text{Zn}^{2+}$  active ions. Compared to G-felt, a few amount of un-etched Zn metal is present in the C-paper anode surface (Fig. S6b), whereas in G-foil, almost no remaining deposited metallic Zn has been seen except an accumulation in the top part of the electrode which could be attributed to the effect of a non-favorable fluid hydrodynamics situation at the vicinity of the sealing gasket.

To sum up, we might state that observing higher discharge capacity of graphite foil is due to the uniform Zn electrodeposition and its planar nature. In brief, the nature of Zn metal deposition is crucial with respect to factors such as the porous structure of the anode and higher applied current. As Yufit et al.<sup>29</sup> reported that generally in the porous electrode, for example, in G-felt, deposition starts to form from the back contact of the electrode by filling all the pores and then it grows further to the electrode surface. During the discharge process, the deposited products etch-back from the electrode bulk. Higher applied current results in higher localized current gradient, which promotes inhomogeneous dissolution from bulk. Hence, in the consecutive cycles, the new products deposit over the already present, un-etched deposition. This deposited layer covers the bulk of the electrode upon cycling, which impacts on the cell electrochemical performance by fading discharge capacity and overall cell efficiency (energy efficiency). The electrochemical performance of the cell assembled with G-felt anode (Fig. 3) and the digital images of cycled G-felt anode (Figs. S6-a, S6-a-i) strongly prove this statement. Whereas comparing the electrochemical full-cell performance and digital images of G-felt with the G-foil, we

could state that Zn metal deposition/dissolution process occurs in an almost reversible manner in planar, graphite foil anode.

**Electrochemical full-cell performance of Zn metal foil as anode.**—In order to prove that when using carbonaceous anodes “Zn dissolution” during discharge plays a vital role on the cycling performances of the cell, restricting the cell discharge capacity, we carried out the full-cell charge/discharge and cycling performances of a cell assembled with highly conductive, Zn metal foil and G-felt as anode, with all other test parameters were kept the same with previous full-cell tests.

Figure 5a shows an excellent discharge capacity among the results shown with the carbonaceous anodes. It is clear from Fig. 5b that this cell is exhibiting excellent coulombic efficiency, with almost 100% capacity retention throughout the cycling, along with very well consistent voltage and energy efficiencies. Apart from having planar structure and high conductivity, the reason for achieving high discharge capacity might be attributed to the no shortage of redox-active  $\text{Zn}^{2+}$  ions with cycling at the anode half-cell. As the eventual deficiency of  $\text{Zn}^{2+}$  ions might happen because of the continuous and not fully reversible deposition/dissolution process, here it can be covered up by the participation of Zn metal foil as the anode. Hence, by comparing the full-cell cycling efficiencies of the cell with porous G-felt (Fig. 3) with this cell with Zn foil, it is clear that Zn is the limiting factor which restricts the battery to reach high discharge capacity by losing active  $\text{Zn}^{2+}$  ions in the metallic form, remaining in the electrode without etching back during the discharge process.

## Conclusions

Herein, we investigated the impact of different anode materials in ZIFB electrochemical performances. We have found that in the anode material, few factors play a crucial role to achieve excellent and stable cycling efficiencies through reversible Zn metal deposition and dissolution. They are their physical structure (such as porous, planar), electrolyte wettability and electrical conductivity. From the full-cell electrochemical evaluation we have found that, compared to porous structures such as graphite felt and carbon paper with high electrochemical surface areas associated to the different microstructures, a planar graphite foil anode exhibits the best capacity retention, due to more reversible zinc plating/stripping process, while maintaining the

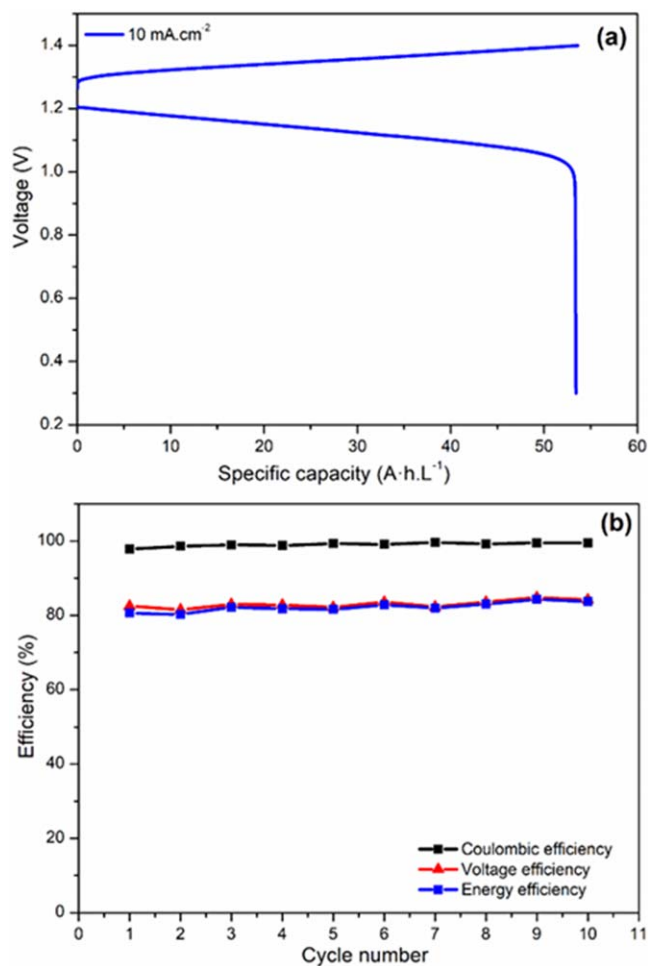


**Figure 5.** Full-cell performance of Zn foil as anode and G-felt as cathode with 1.5 M  $\text{ZnI}_2$ : KI (1:1) at a current density of  $10 \text{ mA}\cdot\text{cm}^{-2}$ . (a) charge-discharge voltage curve and (b) cycling performances for efficiencies of the cell.

lowest internal resistance and consistently high-efficiency values. These results are also associated to the combined hydrophilic nature and highly graphitized structure, which ultimately guarantee high wettability and lower ohmic resistances. We obtained similar results with a Zn foil anode, proving that Zn is a limiting element affecting the cell capacity while having a porous structure is not a necessary requirement for reaching high efficiencies.

In this work of Zn-iodide flow batteries, we have developed a statement about the influence of the structure of the anode materials towards achieving excellent full-cell electrochemical performance, which might further enlighten a path for efficient cyclability of ZIFBs by selecting best-performed anode. Moreover, the cell potential attained during the charge with the planar electrode shows relatively low overall losses vs the thermodynamic value (1.299 V), which lies below the practical water electrolysis voltage ( $>2 \text{ V}$ ). Hence, this system is a potential excellent candidate to couple with photoelectrodes, aiming at developing next-generation solar charging batteries.

## Acknowledgments

The authors thank Generalitat de Catalunya for financial support through the CERCA Program and M2E (2017SGR1246). IREC also acknowledges support by the European Regional Development Funds (ERDF, FEDER) and by MINECO project WINCOST ENE2016-80788-C5-5-R. M.C. has received funding from the European Union's Horizon 2020 research and innovation programme under the Marie Skłodowska-Curie grant agreement No 754397. M.C. acknowledges the doctoral programme "Programa de Doctorat en Ciència de Materials de la UAB." Authors thank Dr. Marc Nuñez, Martí Biset-Peiro and Dr Simone Anelli for assisting to the Raman Spectroscopy and contact angle measurements.

## ORCID

Sebastián Murcia-López  <https://orcid.org/0000-0002-3703-041X>

## References

1. J. A. Turner, *Science*, **285**, 687 (1999).
2. T. Nguyen and R. F. Savinell, *The Electrochemical Society Interface*, **19**, 54 (2010).
3. A. Z. Weber, M. M. Mench, J. P. Meyers, P. N. Ross, J. T. Gostick, and Q. Liu, *J. Appl. Electrochem.*, **41**, 1137 (2011).
4. G. L. Soloveichik, *Chem. Rev.*, **115**, 11533 (2015).
5. Z. Yang, J. Zhang, M. C. W. Kintner-Meyer, X. Lu, D. Choi, J. P. Lemmon, and J. Liu, *Chem. Rev.*, **111**, 3577 (2011).
6. M. Skyllas-Kazacos, M. Rychcik, R. G. Robins, A. G. Fane, and M. A. Green, *J. Electrochem. Soc.*, **133**, 1057 (1986).
7. M. Skyllas-Kazacos and F. Grossmith., *J. Electrochem. Soc.*, **134**, 2950 (1987).
8. M. Skyllas-Kazacos, M. H. Chakrabarti, S. A. Hajimolana, F. S. Mjalli, and M. Saleem, *J. Electrochem. Soc.*, **158**, R55 (2011).
9. S. Biswas, A. Senju, R. Mohr, T. Hodson, N. Karthikeyan, K. W. Knehr, A. G. Hsieh, X. Yang, B. E. Koel, and D. A. Steingart, *Energy Environ. Sci.*, **10**, 114 (2017).
10. B. Li, Z. Nie, M. Vijayakumar, G. Li, J. Liu, V. Sprenkle, and W. Wang, *Nat. Commun.*, **6**, 1 (2015).
11. M. Davies and E. Gwynne, *JACS*, **74**, 2748 (1952).
12. J. C. Verhoef and E. Barendrecht, "Electrochemical behaviour of iodide at a rotating platinum disk electrode in methanol." *Electrochim. Acta*, **23**, 433 (1978).
13. G. M. Weng, Z. Li, G. Cong, Y. Zhou, and Y. C. Lu, *Energy Environ. Sci.*, **10**, 735 (2017).
14. B. Li, J. Liu, Z. Nie, W. Wang, D. Reed, J. Liu, P. McGrail, and V. Sprenkle, *Nano Lett.*, **16**, 4335 (2016).
15. H. Pan et al., *ACS Energy Lett.*, **2**, 2674 (2017).
16. C. Bai, F. Cai, L. Wang, S. Guo, X. Liu, and Z. Yuan, *Nano Res.*, **11**, 3548 (2018).
17. Y. Li, L. Liu, H. Li, F. Cheng, and J. Chen, *Chem. Commun.*, **54**, 6792 (2018).
18. C. Xie, H. Zhang, W. Xu, W. Wang, and X. Li, *Angewandte Chemie - International Edition*, **57**, 11171 (2018).
19. C. Xie, Y. Liu, W. Lu, H. Zhang, and X. Li, *Energy Environmental Science*, **12**, 1834 (2019).
20. J. Zhang, G. Jiang, P. Xu, A. G. Kashkooli, M. Mousavi, A. Yu, and Z. Chen, *Energy & Environmental Science*, **11**, 2010 (2018).
21. S. Ito, M. Sugimasa, Y. Toshimitsu, A. Orita, M. Kitagawa, and M. Sakai, *Electrochim. Acta*, **319**, 164 (2019).
22. K. Lu, H. Zhang, B. Song, W. Pan, H. Ma, and J. Zhang, *Electrochim. Acta*, **296**, 755 (2019).
23. M. Chamoun, B. J. Hertzberg, T. Gupta, D. Davies, S. Bhadra, B. Van Tassell, C. Erdonmez, and D. A. Steingart, *NPG Asia Mater.*, **7**, e178 (2015).
24. H. R. Jiang, M. C. Wu, Y. X. Ren, W. Shyy, and T. S. Zhao, *Appl. Energy*, **213**, 366 (2018).
25. S. Hosseini, A. Abbasi, L. O. Uginet, N. Haustraete, S. Praserthdam, T. Yonezawa, and S. Kheawhom, *Sci. Rep.*, **9**, 1 (2019).
26. Y. Ashraf Gandomi, D. S. Aaron, J. R. Houser, M. C. Daugherty, J. T. Clement, A. M. Pezeshki, T. Y. Ertugrul, D. P. Moseley, and M. M. Mench, *J. Electrochem. Soc.*, **165**, A970 (2018).
27. F. Tuinstra and J. Koenig, *J. Chem. Phys.*, **53**, 1126 (1970).
28. O. A. Maslova, M. R. Ammar, G. Guimbretière, J. N. Rouzard, and P. Simon, *Physical Review B - Condensed Matter and Materials Physics*, **86**, 1 (2012).
29. V. Yufit, F. Tariq, D. S. Eastwood, M. Biton, B. Wu, P. D. Lee, and N. P. Brandon, *Joule*, **3**, 485 (2019).